Model of the low temperature magnetic phases of gadolinium gallium garnet

M. Ancliff[1], V. Sachnev[2] and N. d'Ambrumenil[3]

[1] Department of Physics, The Catholic University of Korea, Bucheon, Gyeonggi-Do, South Korea

E-mail: mark.ancliff@catholic.ac.kr

[2] Department of Information, Communication, and Electronic Engineering, The Catholic University of Korea, Bucheon, Gyeonggi-Do, South Korea

[3] Department of Physics, University of Warwick, Coventry CV4 7AL, United Kingdom

Abstract.

The magnetic behaviour of gadolinium gallium garnet in an external magnetic field at zero temperature is considered. For high fields a classical spin model of the gadolinium ions predicts a spin configuration that is periodic at the level of the smallest repeating unit cell. The quantum version of the model is treated via a truncated Holstein-Primakoff transformation with axes defined by the classical spin configuration, and the magnon excitation bands are calculated. The model predicts a transition in the field range of 1.9—2.1 T, sensitive to the direction of the applied field, which is caused by one or more magnon modes becoming soft as the field is decreased. In general the soft modes occur at incommensurate wavevectors and therefore break the periodicity of the spin configuration below the transition. One exception occurs when the field aligns with one of the principle crystal axes, in which case periodicity of the spin configuration is found to be maintained on a larger crystallographic cubic cell even below the transition. This simple case is studied in more detail. Comparisons are drawn with existing experimental data, and further experimental tests of the model are suggested.

Keywords: Frustrated magnetism, Magnetic phase transitions, spinwaves

1. Introduction

Gadolinium gallium garnet ($Gd_3Ga_5O_{12}$) has attracted interest as a frustrated anti-ferromagnetic crystal displaying a large number of different magnetic phases as a function of temperature and applied magnetic field [1, 2, 3, 4, 5]. At low external fields and intermediate temperatures the system displays a spin-liquid phase with hidden long-range order found in the spin configurations around 10-site rings of gadolinium ions [6]. The system undergoes an unconventional spin-glass transition as the temperature is lowered below around 0.15 K [7, 8, 9], whose nature is not completely understood, but which has been suggested to be related to a change in the ordering around the same 10-site rings [10]. At large fields (around 1.8 T and above) there is a paramagnetic phase in which spins are closely aligned with the magnetic field, with some periodic canting due to the spin-spin interactions [11].

The behaviour of the system between the spin-liquid and paramagnetic phases has been probed by measurements of magnetic susceptibility[1, 12], specific heat and thermal expansion[2, 3], neutron diffraction[4, 13, 14, 15], and sound velocity and attenuation[5]. These experiments reveal several intermediate field-induced antiferromagnetic phases, some of which display spin ordering incommensurate with the lattice, but which cannot be explained in terms of a single spin-wave [11, 15]. Much is still unknown about the magnetic ordering in these intermediate phases, but evidence shows they are sensitive to the direction of the applied magnetic field relative to the crystal axes [1]. This strong anisotropy of the phase diagram has been most clearly shown in comparisons of the cases with $B||(001)$ and $B||(110)$, which can be found in [5], [13], and [15].

This paper presents a theoretical study of the magnetic order and magnon excitation spectra in the high-field paramagnetic phase, and their role in the transition to the intermediate phase immediately below it, at zero temperature. The long-range dipolar forces are found to play a critical role in the nature of the transition and this is suggested as an explanation for the anisotropy seen in the phase diagram. The theoretical model is introduced in section 2. The analysis in the high field regime is simplified as the spin configurations are known to be periodic at the level of the smallest repeating unit cell of the garnet lattice. In section 3 the nature of the transition into the intermediate phase at lower applied fields is studied, and is found to be caused by the softening of one or more magnon modes in the paramagnetic phase. The critical field and the wavevector of the soft modes depend on the field direction and, in the case of $B||(110)$, a whole line of modes is found to go soft at approximately the same field. For most field directions the soft modes occur at wavevectors incommensurate with the reciprocal lattice, which breaks the periodicity and suggests the creation of incommensurate spinwaves below the transition. The case of $B||(001)$ is unusual in that a single magnon mode goes soft at the H-point of the first Brillouin zone, suggesting that the spin ordering may remain commensurate with the lattice below the transition, which allows a more detailed examination of this case in section 4. The results of the model are compared with the known experimental results, and suggestions are made for neutron scattering measurements which could further test the predictions of the model.

2. Theoretical model and methods used

The spin-states of the Ga^{2+} and Gd^{3+} ions in gadolinium gallium garnet are $S = L = 0$ and $S = 7/2, L = 0$ respectively. Thus, magnetic properties of gadolinium gallium garnet are driven by the Gd^{3+} ions, which display significant antiferromagnetic exchange and long-range dipolar interactions. The gadolinium ions lie on a garnet lattice, belonging to the BCC crystal class, with 12 gadolinium ions per smallest repeating unit cell, henceforth referred to as the BCC unit cell. The smallest repeating *cubic* cell of the lattice, with double the volume of the BCC unit cell, has side length $a_0 = 12.35$Å [8], and in what follows is referred to as the unit cubic cell.

The nearest neighbour graph of the gadolinium ions shows two unconnected sublattices composed of equilateral triangles connected at the vertices. The nearest neighbour antiferromagnetic interactions therefore give rise to frustration. The two sublattices are coupled by interactions of third-nearest neighbours and the dipole-dipole interaction. See figure 1 for a representation of the lattice structure and interactions.

Adiabatic susceptibility measurements [16] suggest an effective Hamiltonian with Zeeman, antiferro-

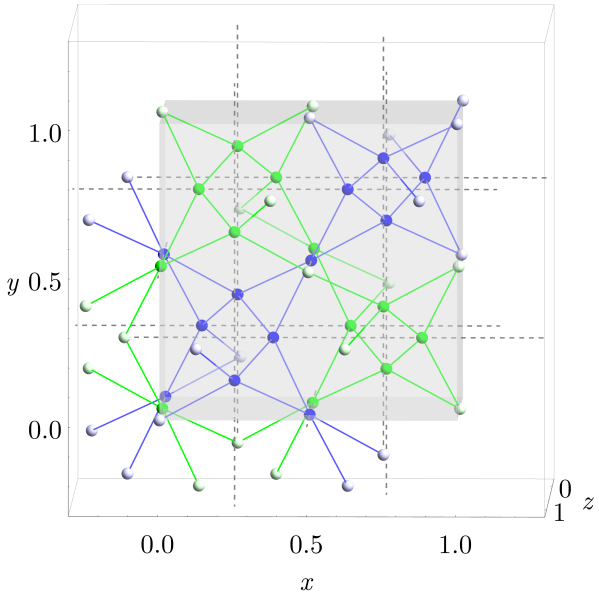

Figure 1. Positions of the gadolinium ions in gadolinium gallium garnet. The nearest neighbour graph splits into two disconnected sublattices, here shown in blue and green. The unit cubic cell is shaded and contains 24 gadolinium sites (sites outside the cell are coloured in lighter hues). Spins on the two sublattices are connected only by third nearest neighbour interactions (shown as dashed gray lines), and the dipolar interactions.

magnetic, and dipolar terms,

$$H = -g\mu_B \mathbf{B}\cdot\sum_j \mathbf{S}_j + \frac{1}{2}\sum_{\substack{i,j\\ i\neq j}} J(|\mathbf{r}_{ij}|)\mathbf{S}_i\cdot\mathbf{S}_j + \\ + \frac{D}{2}\sum_{\substack{i,j\\ i\neq j}}\left(\frac{\mathbf{S}_i\cdot\mathbf{S}_j}{|\mathbf{r}_{ij}|^3} - 3\frac{(\mathbf{S}_i\cdot\mathbf{r}_{ij})(\mathbf{S}_j\cdot\mathbf{r}_{ij})}{|\mathbf{r}_{ij}|^5}\right), \qquad (1)$$

where $J(|\mathbf{r}_{ij}|)$ determines the strength of spin-spin interactions, and only interactions between first-, second-, and third- nearest neighbors are assumed to be significant. The model assumes the spins are isotropic (the large, pure spin state of the gadolinium ions should minimize the effect of the crystal field). Experimental measurements have provided an upper-bound on the single-ion spin anisotropy of 0.04 K [17].

The value of the dipolar interaction strength is $D{r_{nn}}^{-3} = 0.046\,\mathrm{K}$ where r_{nn} denotes the nearest-neighbour distance. Best-fit values for the coupling constants were found to be $J_1 = 0.107\,\mathrm{K}$, $J_2 = -0.003\,\mathrm{K}$ and $J_3 = 0.013\,\mathrm{K}$, though the study found significant uncertainty in the values of J_1 and J_2 as a function of J_3 [16]. A later study refined the values of $J_2 = -0.005\,\mathrm{K}$ and $J_3 = 0.010\,\mathrm{K}$ using neutron scattering data and assuming the same value for J_1 [18]. The difference in the quoted values of J_2 and J_3 have minimal impact on the findings presented in this paper.

Models with the Hamiltonian (1) have been employed in Monte-Carlo simulations [6, 14, 12, 19] and mean-field treatments [18, 20] of the system, which have been used to probe both the low-field spin-liquid and high-field paramagnetic phases of the system. In the high-field phase the model has been shown to be capable of explaining puzzling experimental findings such as the appearance of non-ferromagnetic Bragg peaks in neutron scattering experiments [11]. However, the Monte-Carlo simulations cited above relied on short-range cutoffs of the dipolar term (at third- or fourth- nearest neighbours) which has the potential to lead to significant errors, especially given the importance of the dipolar term in determining the spin-ordering below the transition. (See also the sensitivity of simulations of the zero-field phase to finite range cutoffs reported in [20].) In this paper the dipolar term is evaluated using the Ewald method [21, 22, 23] to avoid these issues.

Before describing the full model it is useful to discuss the simplified case with no dipolar or spin-spin interactions beyond the nearest neighbour. Here the model displays complete rotational symmetry (a simultaneous rotation of all spins and Zeeman term commutes with the Hamiltonian), so the direction of the crystal axes with respect to that of the magnetic field is unimportant, and the fully ferromagnetic state with all spins aligned with the external field is an eigenstate of the Hamiltonian. The magnon spectrum from this eigenstate shows that the lowest-energy excitations form a 4-fold degenerate flat band, due to the existence of perfectly localized excitations around the 10-site rings mentioned above [11, 24]. The ferromagnetic eigenstate is found to be stable to magnon-excitations down to a field of around 1.7 T, where the degenerate flat bands go soft. Including either dipolar or further spin-spin interactions into the model destroys the exact localization of the excitations and distorts the bands. The dipolar term also breaks the rotational symmetry and means that the ferromagnetic state is no longer an exact eigenstate of the Hamiltonian.

The large spin of the Gd^{3+} ions suggests that a classical spin model is a reasonable starting point. We take spins of length 7/2, and use the Hamiltonian (1) with the values from [16]. It is assumed that the spin configuration in the ground state of the high-field phase has the same periodicity as the lattice. This assumption is supported by neutron scattering data for integer peaks such as (111) and (210), which are ruled out for configurations which are periodic on the level of the BCC unit cell. Experimentally, such peaks are absent in the high-field phase but appear below the transition [4, 11]. To further test this assumption we performed numerical optimization on systems up

to 30 × 30 × 30 unit cubic cells in the high-field phase. In each case a unique minimal energy state was found in which each BCC unit cell had identical spin configuration, as assumed. See Appendix A for more details.

Above the transition, an approximate ground-state for the quantum system and corresponding magnon excitation spectrum are calculated using linear spinwave theory, following a similar method to that presented in [25]. First the classical ground-state spin configuration for a single BCC unit cell with periodic boundary conditions is calculated numerically. Local axes $(\mathbf{e}_i^x, \mathbf{e}_i^y, \mathbf{e}_i^z)$, are chosen at each site (i=1,...,12) of the BCC unit cell, so that the local z-axis is aligned with the classical ground-state spin at the same site. A Holstein-Primakoff transformation based upon these axes is then applied to the quantum Hamiltonian, truncated at zeroth order in S,

$$\begin{aligned} S^x_{A,i} &\to (S/2)^{1/2}(\hat{a}_{A,i} + \hat{a}^\dagger_{A,i}) \\ S^y_{A,i} &\to -\mathrm{i}(S/2)^{1/2}(\hat{a}_{A,i} - \hat{a}^\dagger_{A,i}) \\ S^z_{A,i} &\to S - \hat{a}^\dagger_{A,i}\hat{a}_{A,i} \end{aligned} \tag{2}$$

where $S = 7/2$ and A indexes the BCC unit cell in the lattice. Fourier transforming the cell index, $a_{A,i} \to a_i(\mathbf{q})$ leads to a Hamiltonian of the form,

$$H = \sum_{\mathbf{q}} \begin{pmatrix} a_i(\mathbf{q}) & a_i{}^\dagger(\mathbf{q}) \end{pmatrix} \begin{pmatrix} h^{\mathrm{ac}}_{ij}(\mathbf{q}) & h^{\mathrm{aa}}_{ij}(\mathbf{q}) \\ h^{\mathrm{cc}}_{ij}(\mathbf{q}) & h^{\mathrm{ca}}_{ij}(\mathbf{q}) \end{pmatrix} \begin{pmatrix} a_j{}^\dagger(\mathbf{q}) \\ a_j(\mathbf{q}) \end{pmatrix} \tag{3}$$

where summation over the site indices i, j is implied. The dipolar and exchange interactions give rise to particle-number non-conserving terms, $(\hat{a}^\dagger_i \hat{a}^\dagger_j$ + h.c.) (such terms arise in the exchange interaction due to the choice of non-parallel local axes). These terms can be removed, and the Hamiltonian diagonalized via a Bogoliubov transformation,

$$\hat{b}_j(\mathbf{q}) = \left(c^i_j \hat{a}_i(\mathbf{q}) + \bar{c}^i_j \hat{a}^\dagger_i(\mathbf{q}) \right) \tag{4}$$

for some coefficients c^i_j and $\bar{c}^i_j$ (note $\bar{c}^i_j$ is not the complex conjugate of c^i_j). The resulting Hamiltonian can be written

$$H = \sum_{\mathbf{q}} \sum_{\alpha=1}^{12} \epsilon_\alpha(\mathbf{q}) \left(\hat{b}^\dagger_\alpha(\mathbf{q}) \hat{b}_\alpha(\mathbf{q}) + \frac{1}{2} \right). \tag{5}$$

The quantum ground state, $\left|\tilde{0}\right\rangle$, is taken to be the state annihilated by all $\hat{b}_i(\mathbf{q})$. The magnon spectrum is then given by the function $\epsilon_i(\mathbf{q})$.

The Ewald technique must be adapted to handle spinwaves with non-zero $\mathbf{q}$ to calculate the correct matrix elements in equation (3). The details are contained in Appendix B, which follows the approaches outlined in [22] and [26]. The fact that in an infinite lattice the sum of the dipolar terms is not absolutely convergent results in a non-analyticity in the matrix elements when $\mathbf{q}$ is equal to a reciprocal lattice vector. As a consequence, some magnon bands become discontinuous at the origin in the thermodynamic limit (see the highest energy bands in figure 4 for an example of this). While this is an interesting phenomenon, by inspection the lowest lying bands do not develop any such discontinuities, and so this effect has no impact on the transition.

From the quantum ground state and magnon spectrum simulated values for elastic and inelastic neutron scattering intensities can be found [27]. The elastic (Bragg) scattering intensity at wavevector $\mathbf{k}$ is calculated as

$$\begin{aligned} &|F(\mathrm{k})|^2 \sum_{i,j} \left(\mathbf{e}^z_i \cdot \mathbf{e}^z_j - (\mathbf{k} \cdot \mathbf{e}^z_i)(\mathbf{k} \cdot \mathbf{e}^z_j)/|\mathrm{k}|^2 \right) \\ &\times \sum_{A,B} \mathrm{e}^{-\mathrm{i}\mathbf{k}\cdot(\mathbf{r}_{A,i} - \mathbf{r}_{B,j})} \left\langle S^z_{A,i} \right\rangle \left\langle S^z_{B,j} \right\rangle, \end{aligned} \tag{6}$$

where $F(\mathrm{k})$ is the magnetic form factor of the Gd^{3+} ions, $\langle \hat{O} \rangle = \left\langle \tilde{0} \right| \hat{O} \left| \tilde{0} \right\rangle$ denotes the ground state expectation of operator $\hat{O}$, and $S^\mu_{A,i}$ is as in equation 2. The inelastic intensity at wavevector $\mathbf{k}$ and energy ϵ is calculated as

$$\begin{aligned} &|F(\mathrm{k})|^2 \sum_{\mu,\nu} \sum_{i,j} \left(\mathbf{e}^\mu_i \cdot \mathbf{e}^\nu_j - (\mathbf{k} \cdot \mathbf{e}^\mu_i)(\mathbf{k} \cdot \mathbf{e}^\nu_j)/|\mathrm{k}|^2 \right) \\ &\quad \times \sum_{A,B} \mathrm{e}^{-\mathrm{i}\mathbf{k}\cdot(\mathbf{r}_{A,i} - \mathbf{r}_{B,j})} \\ &\quad \times \sum_{\mathbf{q}} \sum_{\alpha=1}^{12} \left\langle S^\mu_{A,i} \hat{b}^\dagger_\alpha(\mathbf{q}) \right\rangle \left\langle \hat{b}_\alpha(\mathbf{q}) S^\nu_{b,j} \right\rangle \delta(\epsilon - \epsilon_\alpha(\mathbf{q})), \end{aligned} \tag{7}$$

where $\mu, \nu \in \{x, y\}$.

3. The high-field phase

3.1. Minimum energy classical spin configurations

In the high field phase the classical spins remain closely aligned with the external field, but there is some small angle canting due to the dipolar and antiferromagnetic interactions. Figure 2 shows an example for $B||(001)$ just above the transition.

3.2. Estimation of the critical field

At fields around 2.5 T and above, the lowest magnon band is approximately flat, but the distortion increases significantly as the transition is approached, and at the transition the band goes soft at a particular wavevector $\mathbf{q}$, although for some field directions several modes go soft at approximately the same field. The magnitude of the critical field depends upon its orientation, as shown in figure 3, and is minimum when the field aligns with a crystal axis and maximum when it lies along the (111) direction.

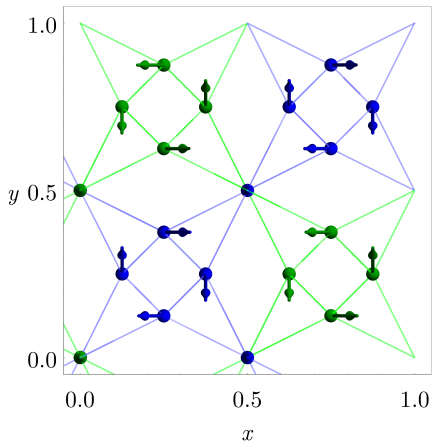

Figure 2. Canting of the classical spins for $B||(001)$ at a field of 2.0 T (just above the transition). The viewpoint is looking down along the z-axis. The spin configurations above the transition share the D_4 point symmetry group of the Hamiltonian, and as a consequence the spins closest to the edges and at the centre of the cell shown are exactly parallel to the field (four additional sites are hidden behind these sites in the projection shown here – compare with figure 1).

.

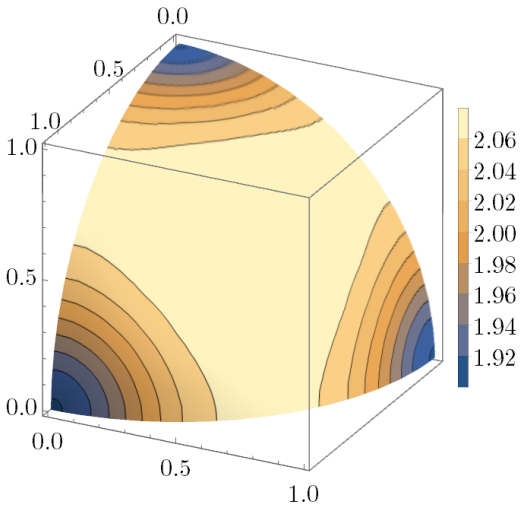

Figure 3. Dependence of the critical field strength on field direction relative to the crystal axes. Field directions are represented as points on the unit sphere, and the contours show the critical field at each point.

3.3. Position of the soft modes: Dependence on field direction and exchange interaction strength

For most directions of the magnetic field the magnon band is found to go soft at an incommensurate wavevector in the vicinity of the H-point of the first Brillouin zone. This implies that the ground state spin configurations of different BCC unit cells will no longer be the same below the transition. In other words the transition is characterized by the appearance of soft magnon modes which break the BCC-periodicity of the spins. Cases $B||(001)$ and $B||(110)$, which have been most thoroughly studied in single-crystal experiments, are unusual in terms of the position of the soft modes. For $B||(001)$ the band is found to go soft exactly at the H-point, whereas for $B||(110)$ a whole line of modes between two H-points go soft at approximately the same field, see figure 4.

The position of the soft mode is found to be sensitive to the D/J_1 ratio as well as the field direction. If the value of the dipolar coupling, D, is decreased to around a third of the estimate given in section 2, the position of the soft mode changes discontinuously – from a position near the H point to a position near the Γ point, as shown in figure 5. This implies that approaches ignoring the dipolar interaction or treating it as a perturbation are unlikely to capture the correct nature of the phase(s) below the transition. Other gadolinium garnets, such as gadolinium aluminium garnet and gadolinium tellurium lithium garnet have the same gadolinium lattice structure but different D/J_1 ratios, and so provide a way to test the dependence of the transition on this ratio [9].

3.4. Comparison with experimental data

Experiments have also found a directional dependence of the critical field, but the field predicted by the model is around 25% above the values found by single-crystal neutron scattering data. Possible reasons for this discrepancy will be discussed in section 5. Specifically, for $B||(0,0,1)$ the critical field predicted by our method is $B_{\text{pred}} = 1.92\,\text{T}$ and that estimated by neutron scattering experiments is $B_{\text{exp}} = 1.5\,\text{T}$ [13]. For $B||(1,1,0)$ the corresponding values are $B_{\text{pred}} = 2.07\,\text{T}$ and $B_{\text{exp}} = 1.67\,\text{T}$ [15]. The ratios $B_{\text{exp}}/B_{\text{pred}}$ are approximately the same in both cases.

The prediction of a second-order transition driven by the softening of magnon modes is consistent with the sharp peaks seen in magnetic susceptibility and specific heat measurements of the transition [2, 4, 12]. Magneto-calorific measurements also show no measurable latent heat associated with the transition (whereas latent heats are observed in the further transitions at lower fields) [3].

Simulated inelastic neutron scattering intensities

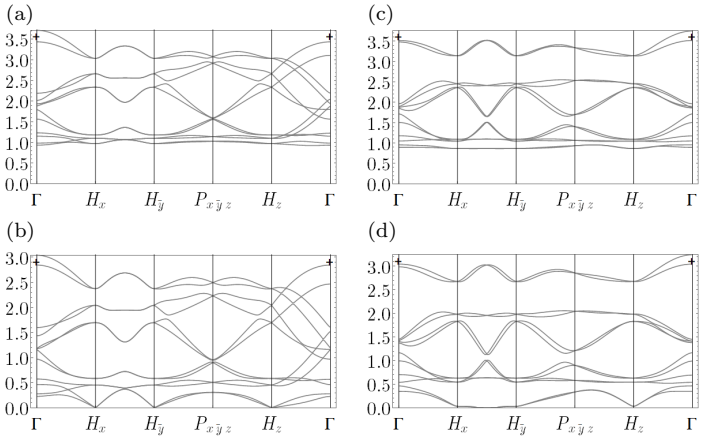

Figure 4. Magnon excitation bands for: (a) $B||(001)$ at 2.5 T, (b) $B||(001)$ at the transition, (c) $B||(110)$ at 2.5 T, (d) $B||(110)$ at the transition. The vertical axis shows excitation energy in Kelvin. For both field directions the lowest band is approximately dispersionless at a field of 2.5 T but develops significant dispersion at the transition. In units of the reciprocal cubic lattice length, $2\pi/a_0$, the labeled points are $H_x = (1,0,0)$, $H_{\overline{y}} = (0,-1,0)$, $P_{x\overline{y}z} = (1,-1,1)/2$, and $H_z = (0,0,1)$ (all H points are equivalent but the directions of approach to them are not). The discontinuity in the energies of some bands as q approaches the Γ point is real – see the text for a discussion. The excitation energies close to, and at, Γ and reciprocal lattice vectors are, however, all well-defined in the thermodynamic limit. In the highest energy band, where the discontinuity is most pronounced, the energy at the Γ point is indicated by a cross.

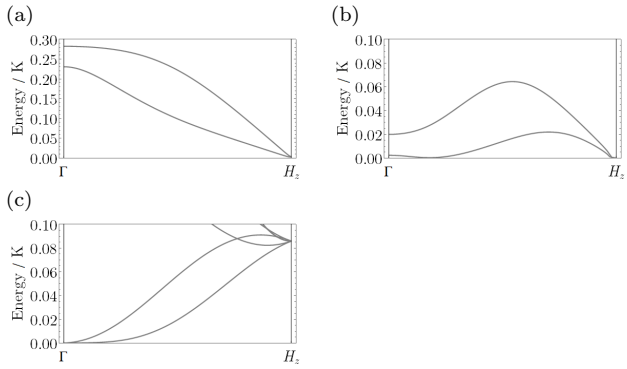

Figure 5. Expanded view of the dispersion of the lowest magnon bands at the transition field for three different values of ${Dr_{nn}}^{-3}$: (a) ${Dr_{nn}}^{-3} = 0.046\,\mathrm{K}$ as stated in the text, (b) ${Dr_{nn}}^{-3} = 0.016\,\mathrm{K}$, and (c) ${Dr_{nn}}^{-3} = 0$ (no dipolar interaction). The position of the soft magnon mode moves discontinuously from the H point to a position near the Γ point as ${Dr_{nn}}^{-3}$ decreases through the value 0.016 (panel b).

suggest that the appearance of the soft mode should be clearly visible as the transition is approached – see figure 6 for the case of $B||(001)$ – which gives another way to test the key prediction of our analysis. We have also calculated simulated inelastic scattering intensities with an average over magnetic field and wavevector directions, to allow comparison with existing data from a powder sample [11]. The result is shown in figure 7 and shows reasonable agreement with the experimental data.

4. Below the transition

The finding that the transition is driven by a soft magnon mode which breaks the periodicity of the spins is consistent with the appearance of Bragg scattering peaks at incommensurate wavevectors seen in neutron scattering experiments below the transition. For $B||(110)$ the soft wavevectors are predicted to be of the form $(1-a, a, 0)$ for $0 < a < 1$, and while single-crystal neutron scattering data is only available for the (kkl) plane, a peak at $(\frac{1}{2}, \frac{1}{2}, 2)$, consistent with the development of a spinwave at $\mathbf{k} = (\frac{1}{2}, \frac{1}{2}, 0)$, has been observed [15]. It should be noted that the same experiment also observed incommensurate peaks at $(1.18, 1.18, 1.32)$, $(-1.53, -1.53, 0.51)$, $(0.59, 0.59, 1.95)$, and $(1.46, 1.46, -0.51)$, which do not correspond to soft-mode wavevectors predicted at the transition. The presence of these additional peaks and the theoretical prediction of many spinwave excitations with very similar low energies at the transition suggest that magnon-magnon interactions are important for understanding the intermediate phase. These interactions have been ignored in our analysis, but are of order $J_1|S|^0 \sim 0.1\,\mathrm{K}$, which is comparable to the energy-width of the lowest band shown in figure 4(d).

If the ground-state classical spin configuration no longer shares the same periodicity as the lattice, the treatment outlined in section 2 requires modification. One option is to assume spin periodicity on a larger scale of several unit cells, and apply the same method to this larger system. However, for general directions of the magnetic field this is not straightforward. Firstly, unlike the paramagnetic phase, where there

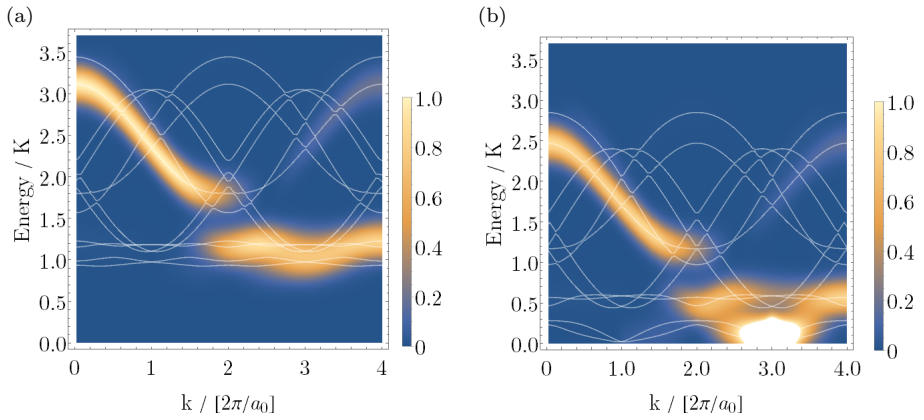

Figure 6. Simulated inelastic neutron scattering intensities for $B||(001)$ at fields of (a) 2.5 T and (b) just above the transition. The scattering wavevector $\mathbf{k}$ runs from the origin to the point $(0, 0, 4)$ in units of $2\pi/a_0$. The positions of the magnon bands are overlayed in white. Strong quasi-elastic scattering is caused by the nearly soft mode at $(0, 0, 3)$ in the second diagram. (The predicted scattering intensity at this point increases by a factor of ten as the transition is approached, as a consequence of an increase in magnitude of the expectations $\left\langle \hat{b}_\alpha(\mathbf{q}) S^\nu_{b,j} \right\rangle$ occuring in equation (7) for the lowest two magnon bands.)

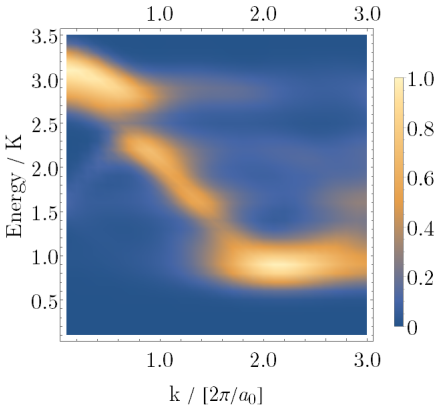

Figure 7. Inelastic scattering intensity at an external field of 2.5 T. Directions of magnetic field and momentum vectors have been averaged over to allow direct comparison to existing experimental data from a powder sample (see [11] fig. 2).

appears to be a unique classical energy minimum, below the transition numerical optimization shows a large number of local energy minima. On lattice sizes large enough to show incommensurate peaks such as those listed in the previous paragraph determining the classical ground state becomes a significant problem. See Appendix A for more details. Secondly, the Bogoliubov transformation and diagonalization of the Hamiltonian (3) required to find the magnon bands also become computationally expensive on these large lattices.

The case when the external field aligns with one of the crystal axes appears to be a special, simple case in this regard. Since for $B||(001)$ the single soft mode appears exactly at the H point of the first Brillouin zone, the spins may remain periodic on the level of the unit cubic cell (with volume double that of the BCC unit cell) even below the transition. In what follows we explore the predictions of the model for $B||(001)$ below the transition using this assumption, applying the methods of section 2 to this larger cell.

4.1. The case $B||(001)$

For fields between the transition (at 1.92T in our approach) and 0.3T, numerical optimization on the unit cubic cell shows there are four degenerate classical spin configurations that (globally) minimise the energy. Similar solutions have been seen before in Monte-Carlo simulations of the same problem [12], and are illustrated in figure 8. Two pairs of these are related by a translation by $\left(\frac{1}{2}, \frac{1}{2}, \frac{1}{2}\right)$, so modulo translations there are only two distinct solutions. These solutions can be mapped into each other by a 90° rotation around the z-axis followed by a translation parallel to the same axis.

Calculations of the magnon spectra show that the magnon excitation energy gap is non-zero except at the transition. This means away from the transition the solution is stable to spinwave excitations and therefore the assumption about the periodicity of the spins below the transition is internally consistent in this regard. The energy of the lowest magnon mode as a function of field strength is shown in figure 9. To further test the assumption of periodicity we performed numerical optimization of the classical spins on lattice sizes up to $20 \times 20 \times 20$ unit cubic cells. While a large number of locally optimal configurations were found, the periodic configurations were found to have the minimum energy of all local optima discovered.

Above the transition the spin configuration is symmetric under 90° rotations around the z-axis (with

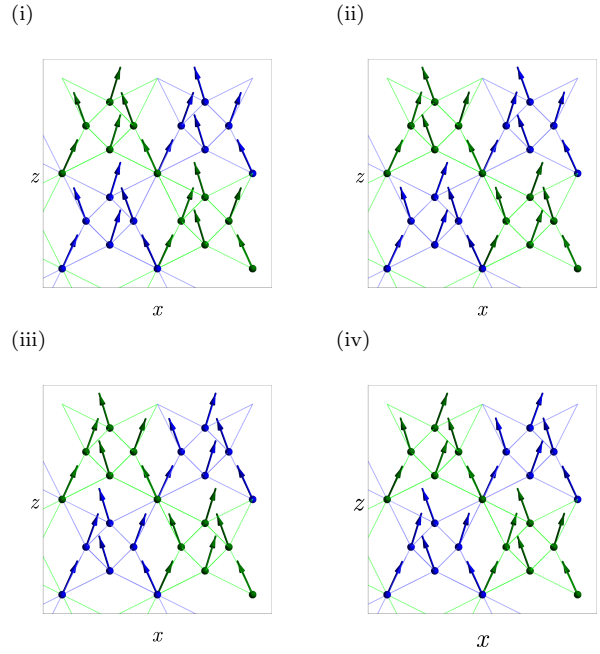

Figure 8. The spin configurations of the four minimum energy solutions at a field of 1.7 T. The first two configurations are equivalent up to translation, as are the last two. The first pair of solutions can be mapped onto the second by a 90° rotation around and translation along the z-axis. The viewpoint is along the x-axis with the z-axis vertical.

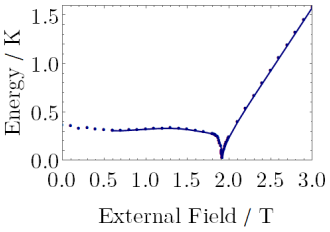

Figure 9. Minimum magnon excitation energy as a function of external field strength for $B||(001)$. The excitation gap falls to zero as the field approaches the transition value of 1.92 T, both from above and from below. Away from the transition at 1.92 T the periodic spin configuration on the unit cubic cell is found to be stable to spinwave excitations, with the energy gap remaining around 0.3 K. Below around 0.5 K, while the spinwave gap remains roughly constant, there exist non-spinwave excitations with lower excitation energy, see the text for more details.

appropriate translation), whereas below the transition this is no longer the case. As a consequence, the two different solutions below the transition generate different scattering profiles for integer wavevectors (klm) with $k \neq l$. Experimental data is available for the (200) peak, and does indeed show two different scattering profiles, labelled according to the direction of field-sweep [13]. It is not clear how the direction of field-sweep should affect the chosen spin configuration, but the profiles found experimentally and those

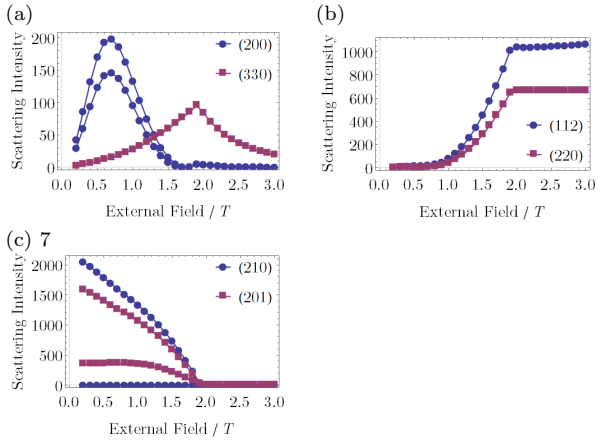

Figure 10. Predicted neutron scattering profiles for: (a) the antiferromagnetic peaks (200) and (330), (b) the ferromagnetic peaks (112) and (220), and (c) the antiferromagnetic peaks (210) and (201). Scattering intensity units are arbitrary but can be compared between graphs. The peaks (200), (210) and (201) show two different profiles corresponding to the two possible spin configurations below the transition, see the text for more details. Experimental data is available for the peaks in (a) and (b) [13].

predicted by our model are in good agreement. The predictions of the model could be further tested by looking at the scattering profiles of the (210) and (201) peaks, which also show significant variation between the two solutions in our model. Predicted scattering profiles for various peaks are shown in figure 10.

Below 1.6 T additional local minima are found in the classical spin configurations. The number of such local minima increases as the field decreases, and hundreds are found for fields less than 0.9 T. The energy gap between these local minima and the ground state decreases as the field decreases, falling below 1 K at a field of 0.6 T and below 0.1 K at a field of 0.2 T. Experimental studies show a second phase transition at a field of around 0.7 T [1, 5]. While the model presented here does not show such a transition, the increasing number of configurations in a narrow band of energies around the ground state is consistent with the development of a spin-liquid phase. Simulations on larger lattice sizes may be able to show this more clearly. We note that in our model the minimum energy classical solutions remain stable to spinwave excitations at low fields, so the transition at 0.7 T cannot be understood in the same way as the transition from the high-field phase, i.e. it does not appear to be driven by a magnon mode becoming soft. This is consistent with experimental evidence of latent heat, suggesting a first order transition [3].

5. Discussion

The treatment of the model presented in this paper gives a description of the transition from the high-field paramagnetic phase of gadolinium gallium garnet to the lower field intermediate phase as a breaking of the BCC-periodicity of the ground-state spins, caused by one or more magnon modes at incommensurate wavevectors becoming soft. The dependence of the critical field and the nature of the intermediate phase on the direction of the magnetic field is shown to be a result of the significant dipole-dipole interactions, which distort the lowest magnon band and thus determine the wavevectors and energies of the minimum energy modes.

Predicted values of the critical field are higher than the experimentally observed values by a factor of approximately 1.25, and agreement with experimental neutron scattering profiles above and below the transition is improved if the external field in the model is linearly scaled by the same factor. The simplest way to account for this difference between theory and experiment would be to change the antiferromagnetic coupling parameters of the model. A reduction of J_1 by around 25% would align the predicted critical fields with those seen in neutron scattering experiments, and also reduces the energy gap between the lowest and highest magnon bands to more closely align with experimental data (compare figure 7 of this paper with figures 2 and 3 of [11]). The value of $J_1 = 0.107\,\mathrm{K}$, used in nearly all theoretical studies to date is based upon [16], which used magnetic susceptibility measurements to impose two non-linear conditions on the parameters (J_1, J_2, J_3). The reported uncertainty in the value of J_1 given the values of the other parameters is rather large, and a 25% reduction of J_1 is (just) consistent with the measurements, provided that the value of J_3 is increased correspondingly (see figure 3 of [16]). Data from subsequent studies which have assumed the value $J_1 = 0.107\,\mathrm{K}$ could probably be used to reduce the uncertainty in the parameter values significantly. Given the vast increase in experimental data for the gadolinium gallium garnet system since these estimates were first made, there is a case to revisit the estimation of the J_1 parameter, for example as was done for J_2 and J_3 in [18].

A previously reported Monte-Carlo simulation of the same system found a similar discrepancy in the predicted and observed critical fields, which was attributed to the effects of quantum fluctuations and disorder in the real physical samples [12]. We can obtain an estimate for the size of quantum effects by comparing the classical $|S| = 7/2$ with the ground state expectation value of the $|\langle \hat{S}^z_{A,i} \rangle|$ predicted by our model. Such a calculation shows a reduction of at most 0.5% above the transition and at most 3% below the transition (for $B||(001)$). While the magnon-magnon interactions corresponding to higher order terms in the Holstein-Primakoff expansion are not included in the model presented here, it seems unlikely that they would be sufficient to explain the observed difference in critical field. A similar treatment of rare-earth ions in a pyrochlore lattice also concluded that quantum corrections were small, although the dipole-dipole interaction was found to increase the size of the fluctuations [25].

As noted above, the inclusion of the dipole-dipole interaction significantly increases the predicted value of the critical field, from approximately 1.7 T in the model with only exchange and Zeeman terms, to around 2.0 T. This is in line with the finding that the dipole interaction generally acts to soften the magnon modes [25]. The Ewald method used here is correct for a spherical sample in a vacuum, and the geometries and environments of real systems will introduce corrections to the calculation [23]. For ellipsoidal crystals the internal magnetic field can be written as $\mathbf{B}_i = \mathbf{B} - \mu_0 \mathbf{N} \cdot \mathbf{M}$ where $\mathbf{M}$ is the magnetization and $\mathbf{N}$ is the magnetic depolarization tensor determined by the geometry. For a spherical crystal, $\mathrm{N} = 1/3$ (scalar), whereas for needle-like crystals such as those used in [12], approximation by an infinitely long cylinder gives $\mathbf{N}$ with eigenvalues $\mathrm{N}_\perp = 1/2$ perpendicular to the long axis and $\mathrm{N}_\parallel = 0$ parallel to the long axis [28]. For a fully polarized crystal we find $\mu_0|\mathrm{M}| \approx 1.0\,\mathrm{T}$ so this gives a maximum difference of around 0.3 T in the internal magnetic field between these two limiting cases. Further work is necessary to fully understand these effects.

One of the most intriguing features of the intermediate-field phases is the existence of strong Bragg scattering peaks seen at several incommensurate wavevectors [15]. The model presented here is unable to provide an explanation for the position and intensities of these peaks. To do so may require dealing with the many nearly-degenerate spin configurations that are found to exist on larger lattices at lower fields. On a smaller scale, extending the model to spin configurations with a periodicity of $2 \times 2 \times 2$ unit cubic cells would enable the study of half-integer peaks also seen in experiments [4, 15].

Acknowledgements

M. A. would like to thank Oleg Petrenko for useful discussions. This research was supported by The Catholic University of Korea Research Fund, 2020, and by the Basic Science Research Program through the National Research Foundation of Korea(NRF), Grant Number 2017R1C1B5017323.

Appendix A. Numerical optimization of the classical spins

This appendix details the numerical method used to find the minimum energy classical spin configurations. The simplest approach used was a greedy optimization algorithm, in which each spin is sequentially aligned to the direction of the local magnetic field. Given a spin configuration $\{\mathbf{S}_i\}$, where one spin, $\mathbf{S}_j$, is allowed to vary and all other spins are fixed, equation (1) implies the energy is minimized when S_j is parallel to the vector,

$$g\mu_B\mathbf{B}\cdot\sum_j\mathbf{S}_j-\frac{1}{2}\sum_{\substack{i\\i\neq j}}J(|\mathbf{r}_{ij}|)\mathbf{S}_i\cdot\mathbf{S}_j \\ -\frac{D}{2}\sum_{\substack{i\\i\neq j}}\left(\frac{\mathbf{S}_i}{|\mathbf{r}_{ij}|^3}-3\frac{(\mathbf{S}_i\cdot\mathbf{r}_{ij})\mathbf{r}_{ij}}{|\mathbf{r}_{ij}|^5}\right). \quad \text{(A.1)}$$

Starting from a random configuration of spins, spins were realigned in this way spin-by-spin until the improvement in energy became negligible, which typically required around a hundred adjustments of each spin.

The results of this optimization were explored for magnetic fields along the symmetry axes (001), (110), and (111), at fields between 0 and 3 T. Cubic lattices of size 1^3, 5^3, 10^3, 20^3, and 30^3 cubic unit cells with periodic boundary conditions were used. For each field, several thousand solutions were generated.

In the high-field paramagnetic phase for fixed field the algorithm always found the same optimal spin configuration, suggesting the existence of a single local optimum. Regardless of field direction this configuration was found to have the periodicity of the BCC unit cell.

In contrast, below the transition a large number of distinct locally optimal spin configurations were discovered. For optimization on a lattice of a single cubic unit cell each solution was found multiple times, and the results were reproducible, suggesting the algorithm was able to discover all locally optimal spin configurations with this periodicity. However, for larger lattice sizes this was not the case. For a given field direction, many hundreds of distinct local optima were discovered and in general we cannot claim with confidence to have located the global optimum. More complex optimization algorithms are currently under investigation but as yet none have been able to consistently identify the ground state.

An example is shown in figure A1, for $B||(110)$, at a field of 1.15 T (chosen to correspond to the maximum of the $(\frac{1}{2},\frac{1}{2},2)$ non-integer peak seen in neutron scattering experiments, [15]), on a lattice of 10^3 unit cubic cells. The local optima occupy a relatively narrow band of energies, but the energy differences between them are significant enough that they do not provide evidence of a highly degenerate ground state. While the different spin configurations all display similar calculated scattering intensities for integer peaks (standard deviations typically within 10% of the mean intensity), they show a large variation in peak intensities at non-integer positions, suggesting a variety of different spin orderings with similar energies.

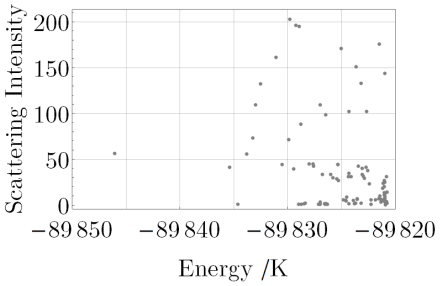

Figure A1. Energies and scattering intensities of the $(\frac{1}{2},\frac{1}{2},2)$ non-integer peak for one hundred solutions on a lattice of 10^3 unit cubic cells, for $B||(110)$ at a field of 1.15 T.

For the case of $B||(001)$ studied in section 4, while a large number of local optima were found on the larger lattice sizes, none of those found had energy lower than that obtained from a periodic extension of the minimum energy solution found on a single cubic unit cell, consistent with the assumption that this is the true global minimum.

Appendix B. Ewald summation for spinwaves

In this section it is shown how the Ewald summation technique for the dipolar term is adapted to allow calculation of the energy of spinwaves. The derivation follows closely that of [22], but it is worth highlighting the origin of the non-analyticity of the magnon energies at the Γ point. A similar analysis has been previously presented in [26].

In what follows, indices A and B label unit cells of the lattice, j and l label the twelve sites in each unit cell, $\mathbf{R}_A$ is the lattice vector of the A-th unit cell, $\mathbf{r}_j$ is the position vector of the j-th site from the cell origin, $\mathbf{r}_{Aj,Bl}=(\mathbf{R}_B+\mathbf{r}_l-\mathbf{R}_A-\mathbf{r}_j)$, and I denotes the 3×3 identity matrix. With this notation, the dipole-dipole interaction term in (1) can be written

$$\frac{D}{2}\sum_{(Aj),(Bl)}\mathbf{S}^\dagger_{Aj}\cdot\left(\frac{I}{|\mathbf{r}_{Aj,Bl}|^3}-3\frac{\mathbf{r}_{Aj,Bl}\,\mathbf{r}^\dagger_{Aj,Bl}}{|\mathbf{r}_{Aj,Bl}|^5}\right)\cdot\mathbf{S}_{Bl} \quad \text{(B.1)}$$

where the self-interaction terms, $(Aj)=(Bl)$, are excluded from the sum.

Now consider a spin configuration on a parallelepided of N unit cells with periodic boundary conditions,

and perform a Fourier transformation of the spin variables:

$$\mathbf{S}_{Aj} = N^{-1/2} \sum_{\mathbf{q}} e^{-i\mathbf{q}\cdot\mathbf{R}_A} \mathbf{S}_j(\mathbf{q}), \tag{B.2}$$

where $\mathbf{q}$ runs over vectors in the first Brillouin zone. Substituting this into (B.1) and setting $\mathbf{r}_{jl} = (\mathbf{r}_l - \mathbf{r}_j)$, results in

$$\frac{D}{2} \sum_{\mathbf{q}} \sum_{j,l} \sum_{\mathbf{R}} \mathbf{S}_j^\dagger(\mathbf{q}) \Bigg[\Bigg(\frac{I}{|\mathbf{r}_{jl}+\mathbf{R}|^3} - 3\frac{(\mathbf{r}_{jl}+\mathbf{R})(\mathbf{r}_{jl}+\mathbf{R})^\dagger}{|\mathbf{r}_{jl}+\mathbf{R}|^5} \Bigg) e^{-i\mathbf{q}\cdot\mathbf{R}} \Bigg] \mathbf{S}_l(\mathbf{q}), \tag{B.3}$$

where R runs over all lattice vectors, and again the self-interaction terms are excluded.

For an infinite lattice, the sum over $\mathbf{R}$ is not absolutely convergent. It can be regularized by the addition of a term $e^{-s|\mathbf{R}|^2}$ with $s > 0$ [22]. Letting $T^{\mu\nu}$ denote the tensor in square brackets in (B.3) with the addition of this regularizing factor, we can write

$$T^{\mu\nu}(\mathbf{r}_{jl}, \mathbf{R}, \mathbf{q}) = -\frac{\partial^2}{\partial \mathrm{r}_{jl}^\mu \partial \mathrm{r}_{jl}^\nu} \left(|\mathbf{r}_{jl}+\mathbf{R}|^{-1} e^{-i\mathbf{q}\cdot\mathbf{R}} e^{-s|\mathbf{R}|^2} \right). \tag{B.4}$$

With the inclusion of the regularizing factor, the sum in (B.3) is absolutely convergent, and the order of differentiation and summation can be exchanged.

The $|\mathbf{r}_{jl}+\mathbf{R}|^{-1}$ term in $T^{\mu\nu}$ can be replaced using the identity

$$r^{-1} = \sqrt{\frac{\epsilon}{\pi}} \int_0^\infty x^{-1/2} e^{-r^2\epsilon x} dx. \tag{B.5}$$

The $\epsilon > 0$ parameter is arbitrary (later it can be chosen to optimize the rate of convergence of the summations). In the Ewald method the resulting integral is split into two halves, on the intervals $(0,1)$ and $(1,\infty)$. On the latter interval, the $s \to 0$ limit can safely be taken and the integral evaluated exactly, leading to the 'space' part of the Ewald sum,

$$T^{\mu\nu}_{\mathrm{space}}(\mathbf{r}_{jl}, \mathbf{R}, \mathbf{q}) = -\frac{\partial^2}{\partial \mathrm{r}_{jl}^\mu \partial \mathrm{r}_{jl}^\nu} \left(\mathrm{erf}\left(|\mathbf{r}_{jl}+\mathbf{R}|^2 \epsilon \right) |\mathbf{r}_{jl}+\mathbf{R}|^{-1} \right) e^{-i\mathbf{q}\cdot\mathbf{R}}, \tag{B.6}$$

where $\mathrm{erf}(\ldots)$ denotes the error function.

On the $(0,1)$ interval, making use of the identity,

$$-s|\mathbf{R}|^2 - \epsilon x|\mathbf{r}_{jl}+\mathbf{R}|^2 = -(\epsilon x + s)\left| \mathbf{R} + \frac{\epsilon x}{\epsilon x + s} \mathbf{r}_{jl} \right|^2 - \frac{\epsilon x s}{\epsilon x + s} |\mathbf{r}_{jl}|^2, \tag{B.7}$$

the sum over lattice vectors $\mathbf{R}$ can be taken inside the integral and transformed to a sum over reciprocal lattice vectors $\mathbf{Q}$. The result is,

$$-\frac{\partial^2}{\partial \mathrm{r}_{jl}^\mu \partial \mathrm{r}_{jl}^\nu} \Bigg[\pi V^{-1} \sqrt{\epsilon} \sum_{\mathbf{Q}} \int_0^1 (\epsilon x + s)^{-3/2} x^{-1/2} \exp[-|\mathbf{Q}+\mathbf{q}|^2/4(\epsilon x + s)] \times \exp[i(\mathbf{Q}+\mathbf{q})\cdot\mathbf{r}_{jl}] \exp[-\epsilon x s |\mathbf{r}_{jl}|^2/(\epsilon x + s)] dx \Bigg] - \frac{4}{3}\pi^{-1/2}\epsilon^{3/2}\delta_{jl}\delta^{\mu\nu}, \tag{B.8}$$

where V is the volume of the unit cell. The last term (outside the square brackets) comes from subtraction of the $\mathbf{R} = \mathbf{0}$, $j = l$ self-interaction terms, which must be added to the sum over $\mathbf{R}$ before transforming to a sum over $\mathbf{Q}$. This is referred to as the 'self' term in the Ewald sum, $T^{\mu\nu}_{\mathrm{self}}(\mathbf{r}_{jl}) = -(4/3)\pi^{-1/2}\epsilon^{3/2}\delta_{jl}\delta^{\mu\nu}$.

Provided that $\mathbf{Q}+\mathbf{q} \neq \mathbf{0}$, there is no divergence in the integral in (B.8) as $s \to 0$. For $s = 0$ the integral can be evaluated exactly to yield $4\epsilon^{-1/2}|\mathbf{Q}+\mathbf{q}|^{-2}\exp[-|\mathbf{Q}+\mathbf{q}|^2/4\epsilon]\exp[i(\mathbf{Q}+\mathbf{q})\cdot\mathbf{r}_{jl}]$, leading to the 'reciprocal' part of the Ewald sum, defined as

$$T^{\mu\nu}_{\mathrm{recip}}(\mathbf{r}_{jl}, \mathbf{Q}, \mathbf{q}) = -4\pi V^{-1} |\mathbf{Q}+\mathbf{q}|^{-2} \exp[-|\mathbf{Q}+\mathbf{q}|^2/4\epsilon] \times \frac{\partial^2}{\partial \mathrm{r}_{jl}^\mu \partial \mathrm{r}_{jl}^\nu} \exp[i(\mathbf{Q}+\mathbf{q})\cdot\mathbf{r}_{jl}], \tag{B.9}$$

when $\mathbf{Q}+\mathbf{q} \neq \mathbf{0}$, and zero elsewhere.

If $\mathbf{Q}+\mathbf{q} = \mathbf{0}$ for some $\mathbf{Q}$ in the reciprocal lattice, then this term in the sum in (B.8) can be transformed via a substitution $u = \epsilon x/(\epsilon x + s)$ into

$$\epsilon^{-1/2} s^{-1} \int_0^{\epsilon/(\epsilon+s)} u^{-1/2} \exp[-su|\mathbf{r}_{jl}|^2] du. \tag{B.10}$$

The divergence of this expression as $s \to 0$ is the origin of the non-analyticity of the magnon bands at a reciprocal lattice vector. Expanding the exponential leads to a Laurent series in powers of s. The divergent s^{-1} term is independent of $\mathbf{r}_{jl}$ and therefore does not contribute to the energy. The s^0 term is $(2/3)\epsilon^{-1/2}|\mathbf{r}_{jl}|^2 + \epsilon^{-3/2}$, and leads to the 'surface' term in the Ewald sum,

$$T^{\mu\nu}_{\mathrm{surf}}(\mathbf{r}_{jl}) = \frac{2\pi}{3V} \frac{\partial^2}{\partial \mathrm{r}_{jl}^\mu \partial \mathrm{r}_{jl}^\nu} |\mathbf{r}_{jl}|^2. \tag{B.11}$$

Putting everything together, (B.3) becomes

$$\frac{D}{2} \sum_{\mathbf{q}} \sum_{j,l} \Bigg[\sum_{\mathbf{R}} T^{\mu\nu}_{\mathrm{space}}(\mathbf{r}_{jl}, \mathbf{R}, \mathbf{q}) + \sum_{\mathbf{Q}} \Big(T^{\mu\nu}_{\mathrm{recip}}(\mathbf{r}_{jl}, \mathbf{Q}, \mathbf{q}) + \delta(\mathbf{Q}+\mathbf{q}) T^{\mu\nu}_{\mathrm{surf}}(\mathbf{r}_{jl}) \Big) + T^{\mu\nu}_{\mathrm{self}}(\mathbf{r}_{jl}) \Bigg] S_j^\mu(\mathbf{q})^\dagger S_l^\nu(\mathbf{q}), \tag{B.12}$$

where summation over μ and ν is implied.

In the actual calculation of magnon bands the sums over $\mathbf{R}$ and $\mathbf{Q}$ were truncated at a few real and reciprocal lattice lengths, respectively. For appropriate choice of ϵ the expected error from this truncation is small (relative error in the

Hamiltonian matrix elements $< 10^{-3}$, see [23] for estimates). Equation (B.12), combined with the truncated Holstein-Primakoff transformations with respect to the local axes of each spin, give the dipolar contribution to the Hamiltonian in equation (3).

References

[1] S. Hov, H. Bratsberg, and A. T. Skjeltorp. Magnetic phase diagram of gadolinium gallium garnet. *J. Mag. Mag. Mat.*, 15-18:455, 1980.

[2] A. P. Ramirez and R. N. Kleiman. Low-temperature specific heat and thermal expansion in the frustrated garnet $Gd_3Ga_5O_{12}$. *J. Appl. Phys.*, 69:5252, 1991.

[3] Y. K. Tsui, C. A. Burns, J. Snyder, and P. Schiffer. Magnetic field induced transitions from spin glass to liquid to long range order in a 3D geometrically frustrated magnet. *Phys. Rev. Lett.*, 82(17):3532, 1999.

[4] P. P. Deen, O. Florea, E. Lhotel, and H. Jacobsen. Updating the phase diagram of the archetypal frustrated magnet $Gd_3Ga_5O_{12}$. *Phys. Rev. B*, 91(1):014419, 2015.

[5] A. Rousseau, J.-M. Parent, and J. A. Quilliam. Anisotropic phase diagram and spin fluctuations of the hyperkagome magnet $Gd_3Ga_5O_{12}$ as revealed by sound velocity measurements. *Phys. Rev. B*, 96(6):060411, 2017.

[6] J. A. M. Paddison, H. Jacobsen, O. A. Petrenko, M. T. Fernández-Diaz, P. P. Deen, and A. L. Goodwin. Hidden order in spin-liquid $Gd_3Ga_5O_{12}$. *Science*, 350(6257):179, 2015.

[7] P. Schiffer, A. P. Ramirez, D. A. Huse, P. L. Gammel, U. Yaron, D. J. Bishop, and A.J.Valentino. Frustration induced spin freezing in a site-ordered magnet: Gadolinium gallium garnet. *Phys. Rev. Lett.*, 74(12):2379, 1995.

[8] O. A. Petrenko, C. Ritter, M. Yethiraj, and D. McK Paul. Investigation of the low-temperature spin-liquid behavior of the frustrated magnet gadolinium gallium garnet. *Phys. Rev. Lett.*, 80(20):4570, 1998.

[9] J. A. Quilliam, S. Meng, H. A. Craig, L. R. Corruccini, G. Balakrishnan, O. A. Petrenko, A. Gomez, S. W. Kycia, M. J. P. Gingras, and J. B. Kycia. Juxtaposition of spin freezing and long range order in a series of geometrically frustrated antiferromagnetic gadolinium garnets. *Phys. Rev. B*, 87(17):174421, 2013.

[10] S. Ghosh, T. F. Rosenbaum, and G. Aeppli. Macroscopic signature of protected spins in a dense frustrated magnet. *Phys. Rev. Lett.*, 101(15):157205, 2008.

[11] N. d'Ambrumenil, O. A. Petrenko, H. Mutka, and P. P. Deen. Dispersionless spin waves and underlying field-induced magnetic order in gadolinium gallium garnet. *Phys. Rev. Lett.*, 114(22):227203, 2015.

[12] P. Schiffer, A. P. Ramirez, D. A. Huse, and A. J. Valentino. Investigation of the field induced antiferromagnetic phase transition in the frustrated magnet: Gadolinium gallium garnet. *Phys. Rev. Lett.*, 73(18):2500, 1994.

[13] O. A. Petrenko, G. Balakrishnan, D. McK Paul, M. Yethiraj, and J. Klenke. Field-induced transitions in the highly frustrated magnet gadolinium gallium garnet — long- or short-range order? *Appl. Phys. A*, 74(Suppl.):S760, 2002.

[14] O. A. Petrenko, D. McK Paul, C. Ritter, T. Zeiske, and M. Yethiraj. Magnetic frustration and order in gadolinium gallium garnet. *Physica B*, 266:41, 1999.

[15] O. A. Petrenko, G. Balakrishnan, D. McK Paul, M. Yethiraj, G. J. McIntyre, and A. S. Wills. Field induced magnetic order in the frustrated magnet gadolinium gallium garnet. *J. Phys.: Conf. Ser.*, 145:012026, 2009.

[16] W. I. Kinney and W. P. Wolf. Magnetic interactions and short range order in gadolinium gallium garnet. *J. Appl. Phys.*, 50(3):2115, 1979.

[17] J. Overmeyer. *Paramagnetic Resonance*, chapter 15. Academic Press, New York, 1963.

[18] T. Yavors'kii, M. Enjalran, and M. J. P. Gingras. Spin hamiltonian, competing small energy scales, and incommensurate long-range order in the highly frustrated $Gd_3Ga_5O_{12}$ garnet antiferromagnet. *Phys. Rev. Lett.*, 97(26):267203, 2006.

[19] O. A. Petrenko and D. McK Paul. Classical heisenberg antiferromagnet on a garnet lattice: A monte carlo simulation. *Phys. Rev. B*, 63(2):024409, 2000.

[20] T. Yavors'kii, M. J. P. Gingras, and M. Enjalran. Ill-behaved convergence of a model of the $Gd_3Ga_5O_{12}$ garnet antiferromagnet with truncated magnetic dipole–dipole interactions. *J. Phys. Condens. Matter*, 19:145274, 2007.

[21] P. P. Ewald. Die berechnung optischer und elektrostatischer gitterpotentiale. *Annalen der Physik*, 369(3):253, 1921.

[22] S. W. de Leeuw, J. W. Perram, and E. R. Smith. Simulation of electrostatic systems in periodic boundary conditions. I. Lattice sums and dielectric constants. *Proc. R. Soc. A*, 373:27, 1980.

[23] Z. Wang and C. Holm. Estimate of the cutoff errors in the Ewald summation for dipolar systems. *J. Chem. Phys.*, 115(14):6351, 2001.

[24] D. L. Bergman, C. Wu, and L. Balents. Band touching from real-space topology in frustrated hopping models. *Phys. Rev. B*, 78(12):125104, 2008.

[25] A. G. Del Maestro and M. J. P. Gingras. Quantum spin fluctuations in the dipolar heisenberg-like rare earth pyrochlores. *J. Phys.: Condens. Matter*, 16:3339, 2004.

[26] M. Enjalran and M. J. P. Gingras. Theory of paramagnetic scattering in highly frustrated magnets with long-range dipole-dipole interactions: The case of the $Tb_2Ti_2O_7$ pyrochlore antiferromagnet. *Phys. Rev. B*, 70(17):174426, 2004.

[27] J. Jensen and A. R. Mackintosh. *Rare Earth Magnetism: Structures and Excitations*. Clarendon Press, Oxford, 1991.

[28] J. A. Osborn. Demagnetizing factors of the general ellipsoid. *Physical Review*, 67(11-12):3351, 1945.